

Geostrophic and Ageostrophic Circulations in Midlatitude Squall Lines

CHUNGU LU*

*Forecast Systems Laboratory, National Oceanic and Atmospheric Administration/Environmental Research Laboratory,
Boulder, Colorado*

PAUL E. CIESIELSKI AND WAYNE H. SCHUBERT

Department of Atmospheric Science, Colorado State University, Fort Collins, Colorado

(Manuscript received 11 January 1996, in final form 14 October 1996)

ABSTRACT

The Eliassen transverse circulation equation is derived from the set of f -plane, semigeostrophic, slab-symmetric equations with the inclusion of both diabatic heating and ambient shear effects. Numerical integrations of this model in geostrophic coordinates are performed in the context of a typical midlatitude squall line characterized by a leading convective line and a trailing stratiform rain region. Some dynamical insights are provided by these integrations in conjunction with the theoretical framework, which seem to be unavailable by primitive-equation model simulations. A more complete dynamical picture of a squall line circulation system is revealed from this study: a balanced midlevel horizontal vortex coupled with an ageostrophic transverse circulation in the normal-line plane. This configuration suggests an interaction between two distinct dynamical scales, that is, the scales with geostrophic and ageostrophic-like motions, both of which play important roles in mesoscale convective systems. The internal and external physical processes that affect the ageostrophic transverse circulation are further discussed.

1. Introduction

An important aspect of modern atmospheric dynamics is the recognition of atmospheric motions with intrinsically distinct scales. Two commonly cited examples of such distinct scale separation are the large-scale synoptic phenomena (e.g., extratropical baroclinic disturbances) and the subcloud convective-scale motions (e.g., 3D turbulence in the atmospheric boundary layer). The former class of motions is strongly influenced by the earth's rotation and possesses quasigeostrophic features, whereas the latter is a highly ageostrophic type of motion in which three-dimensional turbulence is crucial. The mesoscale (i.e., the scale between these two) is characterized by motions in which neither the effect of background rotation nor ageostrophic advection is negligible (Emanuel 1979).

Observational studies of mesoscale convective systems, such as midlatitude squall lines with trailing stratiform precipitation, typically reveal two prominent flow

features: a midlevel warm-core vortex and a mesoscale circulation pattern in the line-normal section (Menard and Fritsch 1989; Houze et al. 1989; Smull and Houze 1987; Rutledge et al. 1988). These squall line features have been studied by large-scale and mesoscale dynamicists and by cloud physicists, with each group approaching the problem from its own unique perspective.

On the one hand, large-scale dynamicists have devoted more attention to the balanced flows in squall lines and have related them to external, large-scale environmental features through slow manifold dynamics. Recent studies using balanced systems such as semigeostrophic theory (Hertenstein and Schubert 1991) and nonlinear balanced equations (Raymond and Jiang 1990; Davis and Weisman 1994; Jiang and Raymond 1995) have examined the midlevel mesovortex in mesoscale convective systems. The study by Hertenstein and Schubert (1991) has shown that the upper-level heating due to condensation and the lower-level cooling due to evaporation of stratiform rain generate a positive potential vorticity (PV) anomaly at lower to midlevels and a negative PV anomaly at upper levels. The balanced flow resulting from these PV anomalies forms a midlevel mesovortex that represents a modification to the large-scale balanced atmosphere that is more permanent than the effects of transient gravity waves (Schubert et al. 1989). The interaction of this vortex with a sheared environment induces further convection

*Joint collaboration with the Cooperative Institute for Research in the Atmosphere, Colorado State University, Fort Collins, CO 80523.

Corresponding author address: Dr. Chungu Lu, Forecast Systems Laboratory, NOAA/ERL, Boulder, CO 80303.
E-mail: lu@fsl.noaa.gov

along the path of the squall line, thus possibly explaining the longevity of certain types of mesoscale convective systems (Raymond and Jiang 1990). An important aspect of these studies is that they allow us to view mesoscale convective systems within the unified theoretical framework of PV dynamics (Hoskins et al. 1985; Haynes and McIntyre 1987). A shortcoming of these studies is their lack of emphasis on the ageostrophic part of the squall line circulation.

On the other hand, mesoscale meteorologists and cloud physicists are more likely to focus on the circulation normal to the squall line, which is largely ageostrophic in nature. Using cloud models (Rotunno et al. 1988; Fovell and Ogura 1988; Weisman 1992), radar (Houze et al. 1989; Rutledge et al. 1988), and other types of conventional observations (Johnson and Hamilton 1988; Gallus and Johnson 1992), they attribute this circulation to internal moist dynamics and microphysics. These studies have identified two major storm-relative flow features in the cross section normal to the squall line: a rear-inflow jet that enters the stratiform rain region and then subsides until it reaches the back edge of the convective line at low levels, and above this rear-inflow jet, a front-to-rear flow emerging from the middle-to-upper part of the convective line. A conceptual model of this internal structure of a mature squall line can be found in Houze et al. (1989).

Although simulations of these squall line flow structures with primitive-equation models (e.g., Fovell and Ogura 1988; Zhang and Gao 1989) compare favorably with observations, the complexity of such models often makes interpretation of their results difficult. On the other hand, Rotunno et al. (1988) and Moncrieff (1978) have developed conceptual models that explain how diabatic heating and ambient shear generate horizontal components of vorticity that result in various types of transverse circulation patterns. Jiang and Raymond (1995) studied both balanced and unbalanced circulations in a mature mesoscale convective system by using a nonlinear balance model. As a complement to their work, the present study uses the semigeostrophic system, which retains ageostrophic advection and a vector vorticity equation, to provide additional dynamical insights into the interaction between the transverse circulation and the midlevel vortex in a squall line. Such a theoretical effort can be accomplished through Eliassen's model (Eliassen 1962). This model has been successfully applied to a variety of problems such as cross-frontal circulation (Eliassen 1962; Hoskins and Draghici 1977), radial circulation in tropical cyclones (Schubert and Hack 1982, 1983), and the Hadley circulation in response to ITCZ forcing (Hack et al. 1989).

The present paper extends the use of Eliassen's model to the study of squall lines in which both diabatic heating and ambient shear are included. In section 2 we derive Eliassen's model from an f -plane semigeostrophic system with slab symmetry and discuss the relevant physical parameters in this model. Following Hoskins and

Draghici (1977), we transform the model into geostrophic space (section 3). Numerical integrations of the transformed Eliassen model are shown in section 4. These results reveal a more complete dynamical picture of a squall line, which contains a balanced midlevel mesovortex and an associated secondary ageostrophic circulation. In addition, the relationship between ageostrophic flows and mesoscale relative jets is examined. In section 5 we discuss the relative importance of internal and external physical processes that may affect the transverse circulation in a squall line.

2. Semigeostrophic transverse circulation equation

a. Governing equations

We consider a typical midlatitude squall line system consisting of a line of convection trailed by an extensive stratiform precipitation region. We assume the squall line has a north-south orientation and moves eastward with a uniform speed U . A Cartesian coordinate system (x, y, z) , which travels with the squall line system, is adopted, with x oriented normal to the line, y along the line, and z the vertical coordinate, defined as $z = [1 - (p/p_0)^\kappa]c_p\theta_0/g$, where subscript zero refers to a surface reference value, p is pressure, θ is potential temperature, c_p is specific heat, and g is gravity. The system-relative coordinate is defined as $x = \bar{x} - Ut$, where \bar{x} is the absolute (ground-relative) coordinate. The corresponding components of the total wind relative to an observer moving with the storm are given by $\mathbf{v} = (u - U, v, w)$. The set of f -plane semigeostrophic equations thus can be written as

$$\frac{Du_g}{Dt} - fv = -\frac{\partial\phi}{\partial x}, \quad (2.1)$$

$$\frac{Dv_g}{Dt} + f(u - U) = -\frac{\partial\phi}{\partial y}, \quad (2.2)$$

$$\frac{\partial\phi}{\partial z} = g\frac{\theta}{\theta_0}, \quad (2.3)$$

$$\frac{\partial u}{\partial x} + \frac{\partial v}{\partial y} + \frac{\partial(\rho w)}{\rho\partial z} = 0, \quad (2.4)$$

$$c_p\frac{D\ln\theta}{Dt} = \frac{Q}{T}, \quad (2.5)$$

where ϕ is the geopotential, T is the temperature, $\rho = \rho_0[1 - (gz/c_p\theta_0)]^{(1-\kappa)/\kappa}$ is the pseudodensity (a known function of z), $D/Dt = \partial/\partial t + \mathbf{v} \cdot \nabla$ is the material derivative, and Q is a bulk diabatic heating that is assumed to be a specified function of space.

b. Geostrophic basic state and two-dimensional simplification

Let us consider a basic state of vertically sheared zonal flow, $(\bar{u}, \bar{v}, \bar{w}) = (\bar{u}_g)(z), 0, 0$ and $\bar{v}_g = 0$, where

the overbar denotes a basic-state field. Assuming that such a basic atmosphere is in geostrophic and hydrostatic balance, then $\bar{u}_g(z)$ and the other basic fields can be determined from

$$\begin{aligned}\bar{u}_g(z) &= -\frac{1}{f} \frac{\partial \bar{\phi}}{\partial y}, \\ \bar{\phi} &= -\int f \bar{u}_g(z) dy + \varphi(z), \\ \bar{\theta} &= \frac{\theta_0}{g} \frac{\partial \bar{\phi}}{\partial z}, \\ \bar{Q} &= 0,\end{aligned}$$

where φ is an arbitrary function. Note that the above basic state is only a function of y, z and exactly satisfies (2.1)–(2.5). In reality, midlatitude squall lines are most likely to occur in an environment with both vertical and meridional shear. In this study, the effect of meridional shear is neglected in accordance with the two-dimensionality assumption that follows.

Because the variability of the dynamics along the line is often small compared with that which occurs normal to the line in a midlatitude squall line system (Ogura and Liou 1980; Smull and Houze 1987), we treat such a line-system as uniform in y . Although the nontrivial and non-constant ambient vertical wind shear¹ is likely to induce y -dependent perturbation fields, we assume that such a deviation from the two-dimensionality is small and hence is neglected. This assumption is justified a posteriori with a scale analysis in section 5. Consequently, any disturbed fields generated by such line-type convection are y -independent; that is, $h(x, y, z, t) = \bar{h}(y, z) + h'(x, z, t)$, where h denotes any dynamic or thermodynamic field. Hereafter, for convenience, the primes are dropped from the perturbed variables. After the decomposition of the total fields into basic and perturbed fields, the governing equations (2.1)–(2.5) reduce to

$$f v_g = \frac{\partial \phi}{\partial x}, \quad (2.1')$$

$$\frac{D v_g}{D t} + f(\bar{u}_g + u_{ag} - U) = -\frac{\partial \bar{\phi}}{\partial y}, \quad (2.2')$$

$$\frac{\partial \phi}{\partial z} = g \frac{\theta}{\theta_0}, \quad (2.3')$$

$$\frac{\partial u_{ag}}{\partial x} + \frac{\partial(\rho w)}{\rho \partial z} = 0, \quad (2.4')$$

$$\frac{D \theta}{D t} = Q - \mathbf{v} \cdot \nabla \bar{\theta}, \quad (2.5')$$

where subscripts g and ag denote geostrophic and ageostrophic, respectively, and where it should now be un-

derstood that $D/Dt = \partial/\partial t + (\bar{u}_g + u_{ag} - U)\partial/\partial x + w\partial/\partial z$, and $Q = (1 - gz/c_p\theta_0)^{-1} Q/c_p$. The geostrophic balance in (2.1') follows from the two-dimensionality assumption, which implies that $u_g = -f^{-1}\partial\bar{\phi}/\partial y = 0$ such that the acceleration term in (2.1) vanishes. Note also that the basic-state Coriolis term and pressure gradient term actually cancel each other in (2.2'), but are retained here in order that all three components of the momentum equation possess a pressure-gradient term so that it is easier to derive a vector vorticity equation in the following subsection. Because the perturbation fields are the primary solutions we are seeking, this governing set constitutes a two-dimensional problem.

c. Conservation principles

We now discuss the conservation relations associated with the simplified set of semigeostrophic equations in order to show that the set is a physically permissible system. Essential physics are revealed in these discussions, providing insights in the interpretation of model results.

- Potential temperature equation is

$$\frac{D \theta}{D t} = Q_{\text{total}}, \quad (2.6)$$

where $Q_{\text{total}} = Q - \mathbf{v} \cdot \nabla \bar{\theta}$. Equation (2.6) states that the perturbation potential temperature following an air parcel is changed through the diabatic heating and the advection of the basic-state potential temperature field by the perturbation winds.

- Vector vorticity equation is

$$\frac{D \boldsymbol{\zeta}}{D t} = (\boldsymbol{\zeta} \cdot \nabla) \mathbf{v} + \boldsymbol{\zeta}_w \frac{\partial \rho}{\rho \partial z} + \mathbf{j} \times \nabla \left(\frac{\partial \bar{\phi}}{\partial y} \right), \quad (2.7)$$

where $\boldsymbol{\zeta} = (-\partial v_g/\partial z, 0, f + \partial v_g/\partial x)$ is the vector vorticity and \mathbf{j} is the unit vector in the y direction. The last term on the right-hand side of (2.7) represents vorticity generation by the ambient shear.

- Ertel potential vorticity equation is

$$\frac{D q}{D t} = \frac{1}{\rho} \boldsymbol{\zeta} \cdot \nabla Q_{\text{total}} + \mathbf{j} \times \frac{1}{\rho} \nabla \left(\frac{\partial \bar{\phi}}{\partial y} \right) \cdot \nabla \theta, \quad (2.8)$$

where $q = (1/\rho) \boldsymbol{\zeta} \cdot \nabla \theta$ is the potential vorticity. From (2.8) we note that q can be generated not only from gradients of diabatic heating but also from various configurations of the basic flow.

- Energy equation is

$$\rho \frac{D}{D t} (K + P) + \nabla \cdot (\rho \mathbf{v} \phi) = f \rho v_g \bar{u}_g - \frac{g}{\theta_0} \rho z Q_{\text{total}}, \quad (2.9)$$

where $K = (1/2)v_g^2$ and $P = -gz\theta/\theta_0$ are the perturbation kinetic and potential energy, respectively. The basic state acts as an infinite reservoir of energy through a continuous conversion of mean potential

¹ Here we consider only unidirectional vertical shear, that is, $\partial \bar{u}_g/\partial z$.

energy into the mean kinetic energy, and then into the eddy kinetic energy through the momentum flux transport process depicted by the first term on the right-hand side of (2.9).

d. The Eliassen transverse circulation equation

Although the governing equations (2.1')–(2.5') form a closed set for the unknowns v_g , u_{ag} , w , θ , and ϕ , they are not in a form convenient for calculation. By this we mean that (2.2') and (2.5') are no longer two independent predictors, because by making use of (2.1') and (2.3'), we note that (2.2') and (2.5') are actually predicting the same quantity (i.e., ϕ). There are several ways to reformulate this system so that it can be conveniently solved. These reformulation procedures involve the elimination of one of the prognostic equations. This has been a subject of several studies in an analogous fashion with quasigeostrophic theory, such as the geopotential tendency form (Schubert 1985), the Q -vector form (Hoskins and Draghici 1977), the potential vorticity with the invertibility principle form (Hoskins 1975; Schubert et al. 1989), and the Eliassen transverse circulation form (Hoskins and Draghici 1977; Schubert and Hack 1983; Hack et al. 1989). In this study, because we are trying to focus on the balanced vortex and its secondary circulation, the best approach is to resort to Eliassen's (1962) method by using the transverse circulation equation to provide a direct physical interpretation.

In deriving the transverse circulation equation, we first define a streamfunction, ψ , by taking into consideration the continuity equation (2.4') such that

$$(\rho u_{ag}, \rho w) = \left(-\frac{\partial \psi}{\partial z}, \frac{\partial \psi}{\partial x} \right). \quad (2.10)$$

Then by combining (2.1') and (2.3'), we obtain the thermal wind relation

$$f \frac{\partial v_g}{\partial z} = \frac{g}{\theta_0} \frac{\partial \theta}{\partial x}. \quad (2.11)$$

Using these two relations, we combine (2.2') and (2.5') by eliminating the local time derivative terms to get

$$\begin{aligned} & \frac{\partial}{\partial x} \left(A \frac{\partial \psi}{\partial x} + B \frac{\partial \psi}{\partial z} \right) + \frac{\partial}{\partial z} \left(B \frac{\partial \psi}{\partial x} + C \frac{\partial \psi}{\partial z} \right) \\ & = \frac{g}{\theta_0} \frac{\partial Q}{\partial x} + 2(\rho C - f^2) \frac{\partial \bar{u}_g}{\partial z}, \end{aligned} \quad (2.12a)$$

where

$$A = \frac{g}{\rho \theta_0} \frac{\partial}{\partial z} (\theta + \bar{\theta}) \quad (\text{static stability}), \quad (2.12b)$$

$$B = -\frac{g}{\rho \theta_0} \frac{\partial \theta}{\partial x} = -\frac{f \partial v_g}{\rho \partial z} \quad (\text{baroclinity}), \quad (2.12c)$$

$$C = \frac{f}{\rho} \left(f + \frac{\partial v_g}{\partial x} \right) \quad (\text{inertial stability}). \quad (2.12d)$$

This diagnostic equation describes the ageostrophic circulation in the (x, z) plane normal to the squall line. The term ‘‘ageostrophic circulation’’ is used because the circulation is composed of ageostrophic flow (u_{ag} , w) and is used as a synonym for secondary circulation or transverse circulation throughout this paper. We see from the right-hand side of (2.12a) that the horizontal differential heating and the basic-state vertical shear force the ageostrophic circulation within the squall line. The second term on the right-hand side of (2.12a) can also be written as $-2g\theta_0^{-1}(\partial\theta/\partial y)(\partial v_g/\partial x)$, which is a simplified form of the x -component of the \mathbf{Q} -vector discussed by Hoskins and Draghici (1977). In terms of the slow manifold dynamics, these ageostrophic flows form a secondary circulation, which is necessary for development of PV anomalies such as those found in Herstein and Schubert (1991). In addition, the static stability, baroclinity, and inertial stability are relevant physical parameters that modulate the ageostrophic flow in a squall line, indicated in (2.12a).

We assume that the perturbation motion fields vanish in the far field and at the bottom and top model boundaries by specifying the Dirichlet boundary conditions

$$\begin{aligned} \psi(x_L, z) &= \psi(x_R, z) = 0, \\ \psi(x, 0) &= \psi(x, z_T) = 0, \end{aligned} \quad (2.12e)$$

where x_L and x_R represent the left and right lateral boundaries, respectively, and z_T is the top of the model. The effect of these boundary conditions is to prevent flow through the boundaries. Therefore, these boundary conditions are only applicable for a large computational domain so that the far fields virtually vanish. The size and resolution of the computational domain are discussed in appendix B.

e. Summary of the balanced model

On the left side of Table 1, (2.6), (2.10), (2.11), and (2.12) form a closed system. However, this system can be further simplified by means of the coordinate transformations that are discussed in the next section.

3. Geostrophic coordinate transformation

Following Hoskins and Draghici (1977), we can transform the set of equations (2.1')–(2.5') to geostrophic coordinates, which are defined as $(X, Z, T) = (x + v_g/f, z, t)$. The detailed derivations are given in appendix A.

TABLE 1. Comparison of the Eliassen model and the transformed Eliassen model.

Eliassen model		Transformed Eliassen model	
$f \frac{\partial v_g}{\partial z} = \frac{q}{\theta_0} \frac{\partial \theta}{\partial x}$	(2.11)	$f \frac{\partial v_g}{\partial Z} = \frac{q}{\theta_0} \frac{\partial \theta}{\partial X}$	(A.14)
$A = \frac{q}{\rho \theta_0} \frac{\partial}{\partial z} (\bar{\theta} + \theta)$	(2.12b)	$\frac{f}{\zeta} = 1 - \frac{1}{f} \frac{\partial v_g}{\partial X}$	(A.6)
$B = -\frac{q}{\rho \theta_0} \frac{\partial \theta}{\partial x} = -f \frac{\partial v_g}{\partial z}$	(2.12c)	$q_T = \bar{q} + q = \frac{q}{\rho \theta_0} \frac{\zeta}{f} \frac{\partial}{\partial Z} (\bar{\theta} + \theta)$	(A.15b)
$C = \frac{f}{\rho} \left(f + \frac{\partial v_g}{\partial x} \right)$	(2.12d)	$s_T = \bar{s} + s = \frac{f}{\rho} \left(f + \frac{\partial v_g}{\partial X} \right)$	(A.15c)
$\frac{\partial}{\partial x} \left(A \frac{\partial \psi}{\partial x} + B \frac{\partial \psi}{\partial z} \right) + \frac{\partial}{\partial z} \left(B \frac{\partial \psi}{\partial x} + C \frac{\partial \psi}{\partial z} \right)$		$\frac{\partial}{\partial X} \left(q_T \frac{\partial \psi^*}{\partial X} \right) + \frac{\partial}{\partial Z} \left(s \frac{\partial \psi^*}{\partial Z} \right)$	
$= \frac{q}{\theta_0} \frac{\partial Q}{\partial x} + 2(\rho C - f^2) \frac{\partial \bar{u}_g}{\partial z}$	(2.12a)	$= \frac{q}{\theta_0} \frac{\partial Q}{\partial X} + 2\rho s \frac{\partial \bar{u}_g}{\partial Z}$	(A.15a)
B.C. $\psi(x_L, z) = \psi(x_R, z) = 0$		B.C. $\psi^*(X_R, Z) = \psi^*(X_L, Z) = 0$	
$\psi(x, 0) = \psi(x, z_T) = 0$	(2.12e)	$\psi^*(X, 0) = \psi^*(X, Z_T) = 0$	(A.15d)
$(\rho u_{ag}, \rho w) = \left(-\frac{\partial \psi}{\partial z}, \frac{\partial \psi}{\partial x} \right)$	(2.10)	$(\rho u_{ag}^*, \rho w^*) = \left(-\frac{\partial \psi^*}{\partial Z}, \frac{\partial \psi^*}{\partial X} \right)$	(A.13)
$\frac{\partial \theta}{\partial t} + (\bar{u}_g + u_{ag}) \frac{\partial \theta}{\partial x} + w \frac{\partial \theta}{\partial z} = Q - v_g \frac{\partial \bar{\theta}}{\partial y} - w \frac{\partial \bar{\theta}}{\partial z}$	(2.6)	$\frac{\partial \theta}{\partial T} + \bar{u}_g(Z) \frac{\partial \theta}{\partial X} + \frac{\theta_0}{g} q_T \rho w^* = Q + \frac{f \theta_0 v_g}{g} \frac{\partial \bar{u}_g}{\partial Z}$	(A.11)

To summarize the transformed model, we now collect equations (A.6), (A.11), (A.13), (A.14), and (A.15), which form a closed system. These equations are summarized on the right-hand side of Table 1. The computational procedure for this system proceeds as follows. Given an initial θ field, we diagnose the along-line geostrophic wind from the thermal wind relation (A.14). We then use (A.6) and (A.15b,c) to compute the circulation parameters potential vorticity (q_T) and inertial stability (s_T). On substituting these results into (A.15a) along with the specified diabatic heating and basic flow fields, we diagnose a streamfunction value at every model grid point. Using (A.13), we determine the ageostrophic flow fields that are used in (A.11) to predict a new θ field and the entire procedure is repeated. Because v_g is known, it is straightforward to use the definition of a geostrophic coordinate to transform the results to physical space. The detailed numerical procedure is described in appendix B.

Comparing the right side of Table 1 with the left, we note some advantages of the transformed model. First, using the transformed coordinate X rather than x results in a stretching of the horizontal coordinate in regions of positive relative vorticity and a shrinking in regions of negative relative vorticity. Second, the total derivative operator in transformed space contains no u_{ag} and U terms. Finally, this transformation results in a simpler transverse circulation equation (A.15a), which contains no cross-derivative terms and where q_T plays the role of static stability and s_T the role of inertial stability. In the transformed coordinate, baroclinity is implicit in the geostrophic coordinate transformation. When vertical shear is present in a simulation, it is possible for the

necessary condition for baroclinic instability to be satisfied. However for the length of integrations (≤ 6 h) used in our simulations, baroclinic instabilities, which grow on longer timescales, do not have sufficient time to develop and affect the results. In general, for stable basic states we have $q_T > 0$ and $\bar{s} > 0$, in which case (A.15a) is elliptic.

4. The balanced flow and coupled transverse circulation

Since the primary focus of the present study is on the dynamical structure of a midlatitude squall line, the microphysics and moisture processes are included implicitly in the specification of the diabatic heating field. This heating field was chosen to represent a steady-state, midlatitude squall line with a trailing stratiform rain region at its mature stage. In particular, the structure and magnitude of the convective and stratiform heating profiles were chosen to qualitatively resemble those obtained by Gallus and Johnson (1991) for the 10–11 June 1985 PRE-STORM squall line. Thus the vertical and horizontal structure of the heating representing the squall line is given by

$$Q(x, z) = Q_c \exp[-\alpha_c^2(x - x_c)^2] \sin^2(\pi z/z_T) + Q_s \exp[-\alpha_s^2(x - x_c - x_s)^2] \sin(2\pi z/z_T), \quad (4.1)$$

where Q_c and Q_s are the maximum rates of convective and stratiform heating, α_c and α_s are the inverse half-widths of the convective and stratiform heating regions, x_c is the position of leading convective line, and x_s is

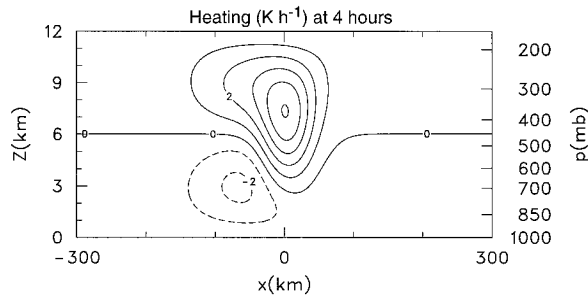


FIG. 1. The diabatic heating field at 4 h, representing a squall line with convective and stratiform precipitation. The leading line is located at $x = 0$. The units are in K h^{-1} with a contour interval of 1 K h^{-1} .

the rearward displacement of the stratiform region behind the convective line. For the simulations presented in this paper we use $Q_c = 4.5 \text{ K h}^{-1}$, $Q_s = -2.5 \text{ K h}^{-1}$, $\alpha_c = (40 \text{ km})^{-1}$, $\alpha_s = (95 \text{ km})^{-1}$, $x_c = 0 \text{ km}$, $x_s = 50 \text{ km}$, $z_T = 12 \text{ km}$, and $U = 10 \text{ m s}^{-1}$, where U is the squall line propagation speed (as defined previously). Figure 1 shows the heating field, which is specified in physical space and then transformed into geostrophic space using the coordinate transformation. The assumption that the heating is not a function of dependent variables implies no direct feedback between the squall line circulation and the heating. Since our intent is to examine the flows induced by a steady heat source in the presence of vertical shear, such a heating parameterization is justified.

Previous studies (Thorpe et al. 1982; Rotunno et al. 1988; Raymond and Jiang 1990) have shown the importance of line-normal vertical shear in maintaining the intensity of the squall line convection. Figure 2 shows the ambient wind profiles chosen for the simulations in this paper. The solid line approximates the profile of line-normal winds observed by Gallus and Johnson (1992) in the presquall environment of the 10–11 June 1985 squall line, featuring strong low-level easterly shear. The magnitude of low-level wind shear in this profile ($12 \text{ m s}^{-1}/3 \text{ km}$) is slightly weaker than the optimal value ($17.5 \text{ m s}^{-1}/2.5 \text{ km}$) used by Rotunno et al. (1988) for maintaining the longest duration of cell updrafts. The steering level (i.e., where $\bar{u}_g = U$) associated with the profile in Fig. 2 is near 550 mb. The deep-layer easterly shear profile (dashed line) approximates that used by Raymond and Jiang (1990). This profile, with a steering level near 300 mb, will be used in a simulation in the next section.

For the model simulations presented here, we use a computational domain that is centered at 35°N and that extends vertically from $Z = 0$ to 12 km and horizontally from $X = -960$ to 960 km . Because of the far-field decay of perturbation motion fields, results are presented only in the near vicinity of the squall line ($-300 \text{ km} \leq X \leq 300 \text{ km}$). The model is integrated by assuming a steady-state squall line (so that the intensity of the

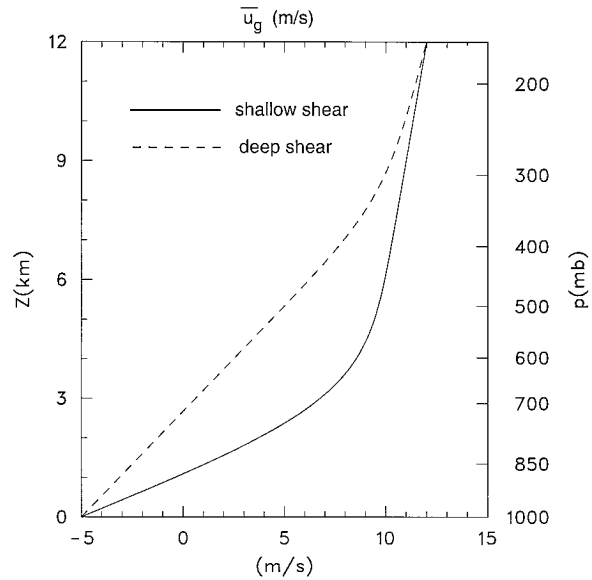


FIG. 2. The ambient wind \bar{u}_g profiles as a function of height. The solid line represents a shallow shear layer profile used in simulations in sections 4 and 5; the dashed line represents a deep shear layer profile used in a simulation in section 5.

heating field does not change with time). The initial θ field is horizontally uniform in X and equal to $\bar{\theta}$. We specify $\bar{\theta}$ by assuming $\bar{\theta}_0 = 290 \text{ K}$ and $d\bar{\theta}/dZ = 4.5 \text{ K km}^{-1}$, which is a good approximation to the 30°N July average temperature from the *U.S. Standard Atmosphere, 1966*. Further model details and the computational procedure are discussed in appendix B. Although the model is integrated in geostrophic space, for ease of interpretation all results are presented in physical space.

Figure 3 shows the balanced along-line wind v_g and circulation parameters q_T and s_T in the normal-line cross section corresponding to the heating field in Fig. 1 and the shallow shear profile in Fig. 2 at $t = 4 \text{ h}$. At this time, the thermally induced flows have reached a quasi-equilibrium state. The physics of the circulation parameters are discussed in the next section. The main features to note in the v_g field are the midlevel cyclonic circulation located between a strong upper-level anticyclone and a weaker low-level anticyclone. An explanation for the evolution of such balanced features is offered by Hertenstein and Schubert (1991). In a case study of a long-lived mesoscale convective system (MCS), Menard and Fritsch (1989) observed an upper-level anticyclone that was inertially unstable and dissipated rapidly. The condition for inertial instability to be present in our model is that $f\zeta < 0$ (or $q_T < 0$). From Fig. 3 (middle panel) we see that values of q_T approach zero above and below the midlevel vortex in regions of anticyclonic shear. However, from (A.6) we note that as anticyclonic shear increases, the normalized absolute vorticity monotonically approaches zero, always remaining positive. Thus, the condition for inertial insta-

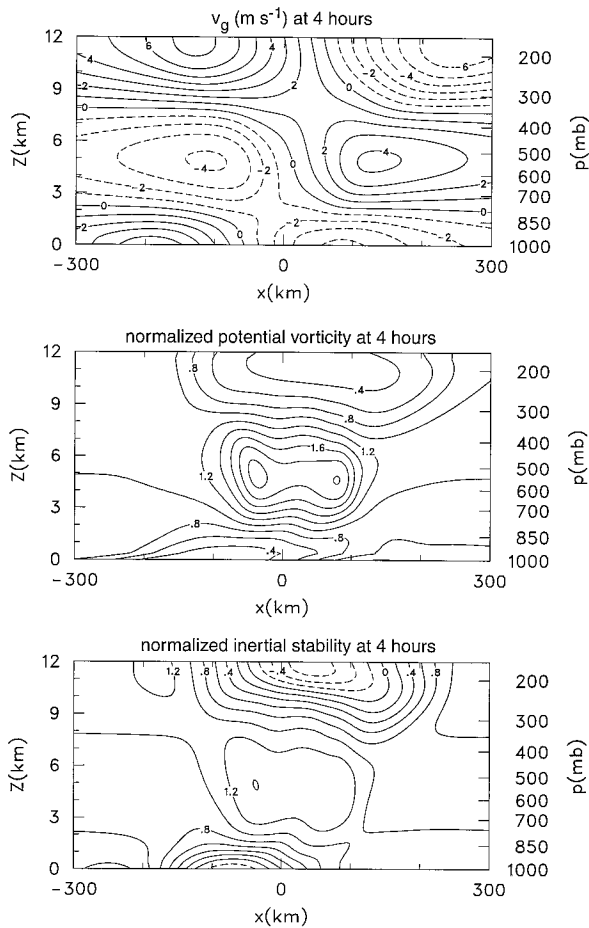


FIG. 3. Results at 4 h using the heating field in Fig. 1 and the shallow shear layer profile in Fig. 2. The top panel shows the along-line balanced wind v_g in m s^{-1} with a contour interval of 1 m s^{-1} . The middle panel shows isopleths of normalized potential vorticity ρq_T in units of $(g/\theta_0)(\partial\bar{\theta}/\partial Z)$ with a contour interval of 0.2. The bottom panel shows isopleths of normalized inertial stability ρs_T in units of f^2 with a contour interval of 0.2.

bility will never be satisfied in our model under anticyclonic shear conditions.

The associated transverse circulation and its two components (the normal-line wind $u_{ag} - U$ and vertical motion w) are shown in Fig. 4. The system-relative transverse circulation exhibits a descending rear inflow, an ascending front-to-rear flow, and divergent outflows near the surface and at upper levels. Viewed together with the balanced circulation in Fig. 3, a clear dynamical scenario of a squall-line system is presented in which the diabatic heating due to the moisture and microphysical processes generates a transverse circulation, which is further modified by the ambient shear. The v_g field develops in response to the transverse circulation as a result of the background rotation; that is, air drawn into the rear of the storm is deflected southward and air drawn into the front of the storm is deflected northward, thus forming the midlevel vortex. A similar argument

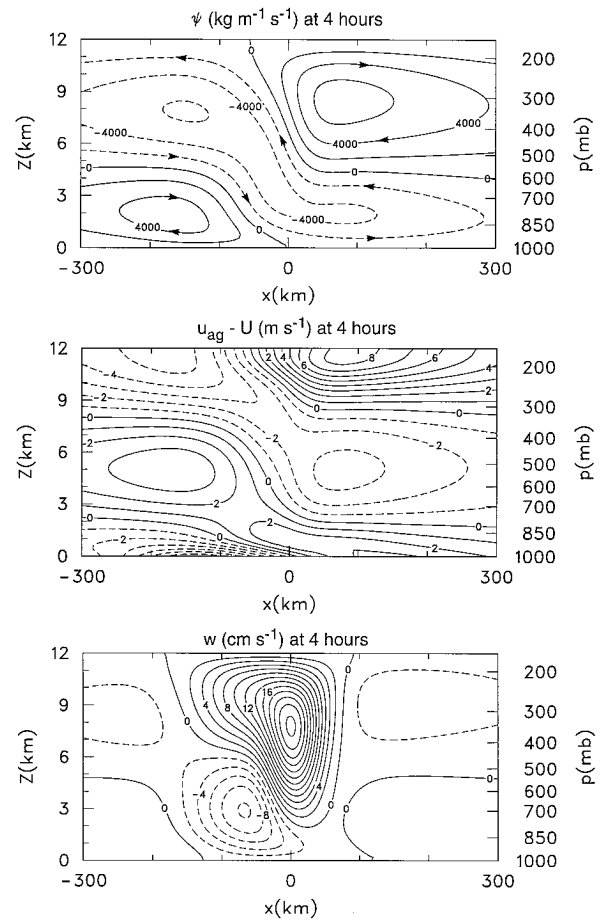


FIG. 4. The transverse circulation that supports the balanced winds in Fig. 3. The top panel is the streamfunction ψ in units of $\text{kg m}^{-1} \text{ s}^{-1}$ with a contour interval of $2000 \text{ kg m}^{-1} \text{ s}^{-1}$. The arrows denote the direction of the flow in the line-normal cross section. The middle panel is the line-normal ageostrophic wind $u_{ag} - U$ (system relative) in m s^{-1} with a contour interval of 1 m s^{-1} . The bottom panel is the vertical velocity w in cm s^{-1} with a contour interval of 2 cm s^{-1} .

follows for the development of the upper- and lower-level anticyclones. As indicated in the theoretical discussions in the previous sections, the transverse circulation is dynamically ageostrophic in nature, whereas v_g is purely balanced flow. Therefore, these two circulations represent an interaction of two distinct dynamical scales of motions. The entire system can be viewed primarily as middle-level vortical motion in the horizontal plane, with a supportive secondary circulation in the vertical plane.

Because of the nature of our balanced model in which the transient inertia-gravity modes have been filtered out, the response of the balanced vortex to the ageostrophic forcing is instantaneous. In reality, of course, there are transient gravity modes. The complete establishment of such a balanced vortex requires time, which is determined by the propagation speed of the internal gravity waves and the local Rossby radius of deformation.

The vertical motion field (see bottom panel of Fig. 4) represents a thermally direct circulation, which is the direct response to the diabatic heating field. Strong upward motion spans the depth of the troposphere near the leading convective line, whereas the updraft and downdraft are decoupled in the upper and lower troposphere in the stratiform region, consistent with the observational study by Biggerstaff and Houze (1991). Another interesting feature is that, although the diabatic heating field is horizontally confined to the near vicinity of the squall-line system (0–200 km), an induced w field spans the entire model domain as a “standing gravity wave.” Although the transient gravity modes are not solutions of our model, the stationary part of these modes do make a weak appearance in the model integration. The mechanism of in-squall line circulation in association with the propagation of gravity waves has been discussed in Schmidt and Cotton (1990).

As discussed previously, the transverse circulation in Fig. 4 contains the major features seen in observational studies (e.g., Houze et al. 1989). However, it should be noted that the flows in Fig. 4 are all relatively small in magnitude. Smull and Houze (1987) observed that the rear inflow in a midlatitude squall line coupled with a stratiform rain region can be rather weak in some storms, while in others it is characterized by a strong, jet-like structure. They suggest two possible mechanisms for rear-inflow jets: 1) acceleration due to the vertical flux of horizontal momentum and 2) acceleration into the midlevel mesolow. Because of the slab symmetry and semigeostrophic assumptions in our model, these mechanisms are outside the physics of our model. Despite the deficiencies of the present model, the strong resemblance between our model-derived transverse circulation and that which is typically observed suggests that the transverse circulation that supports the balanced flow represents an important component of rear-inflow jets and more generally of the entire storm relative flow.

5. The sensitivity of the transverse circulation to external physical processes and circulation parameters

According to (A.15a), the circulation in the x – z plane of a squall line is externally forced by two mechanisms: 1) the horizontal differential heating and 2) the vertical shear of the ambient wind. This flow pattern is also determined by two circulation parameters, namely the potential vorticity and inertial stability.

An estimate of the two external forcing terms for a typical squall line (for example, using a heating rate of a few degrees per hour, a basic-state north–south temperature gradient of 10 K/1000 km, and a relative vorticity on the order of 10^{-4} s^{-1}) shows that, in general, the diabatic forcing is an order of magnitude larger than that associated with the ambient shear. To further quantify this estimate and test the sensitivity of the transverse

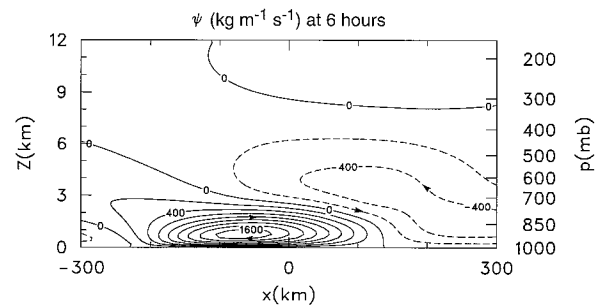


FIG. 5. The streamfunction ψ in units of $\text{kg m}^{-1} \text{s}^{-1}$ with a contour interval of $200 \text{ kg m}^{-1} \text{s}^{-1}$ at 6 h for the simulation with a shallow shear layer and heating set to zero at 4 h. The arrows denote the direction of the flow in the line-normal cross section.

circulation to different shears, we designed the following simulations. In these simulations the model was run with the two wind profiles in Fig. 2 for 4 h. This allowed a substantial balanced flow and associated anomalies of q_T and s_T to develop. The results for the shallow shear case have already been shown (Figs. 3 and 4). Except for minor differences in the balanced wind field v_g and its parameters q_T and s_T , due to the different advective speeds in the two simulations, the results for both types of shear profiles are quite similar. Differences in the transverse circulation (and its components $u_{ag} - U$ and w) are even less apparent. This insensitivity of both balanced and transverse circulation flows to different ambient shear suggests that diabatic heating is a dominant factor in a mature, steady-state storm as far as the strength and structure of the flow are concerned. This is not to say, however, that shear effects are unimportant in the organization of convective storms. As discussed in several of the studies cited previously, vertical wind shear can play a crucial role in initiation and continuation of a mesoscale convective system.

To isolate even further ambient shear effects, we continued the above simulations for an additional two hours with the heating term in (A.15a) set to zero. The mid-level balanced vortex exhibited little change both in its structure and intensity with this experiment (i.e., similar to that in Fig. 3). However, the ageostrophic transverse circulation lost nearly all of its intensity in the absence of diabatic heating. The streamfunction field for the shallow shear case is shown in Fig. 5 (note that the contour level is an order of magnitude smaller than the previous one). The effects of the ambient shear, which maximize where large shear and s_T anomalies coincide, produce a streamfunction field that is generally an order of magnitude less than that at 4 h when the heating was present, as in Fig. 4. The notable exception to this is at the lowest model levels where the strong shear has resulted in a streamfunction amplitude that is comparable to that caused by the heating.

The vertical motion fields for the simulations with shallow and deep vertical shear are shown in Fig. 6. The associated fields of s_T and q_T have the largest pos-

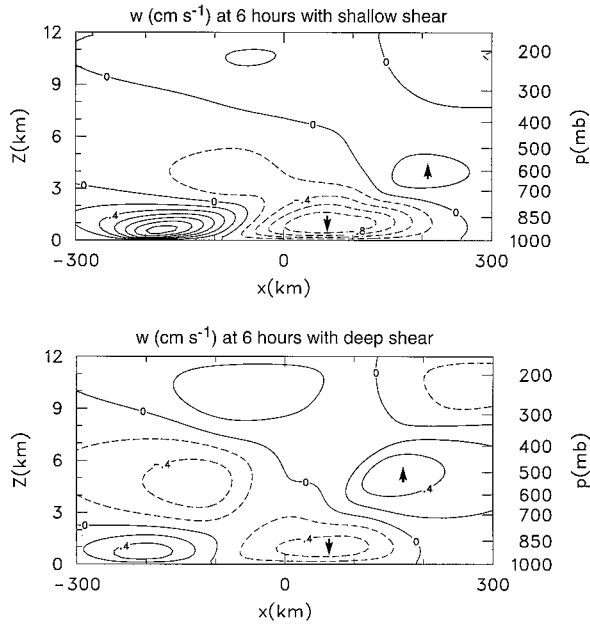


FIG. 6. The vertical velocity w (in cm s^{-1}) with a contour interval of 0.2 cm s^{-1} at 6 h, for the simulation with a shallow shear layer (top panel) and a deep shear layer (bottom panel). Arrows indicate the directions of vertical motions.

itive anomalies (not shown) centered in the midtroposphere near $x = 0 \text{ km}$. Downshear of these anomalies, weak upward motion ($< 0.5 \text{ cm s}^{-1}$) is observed, consistent with quasigeostrophic theory that predicts upward motion on the downshear side of a positive PV anomaly. Raymond and Jiang (1990) suggest that this shear-induced upward motion (which was on the order of 1 cm s^{-1} in their simulation) may trigger or sustain further convection in some types of MCSs. The magnitude of the shear-induced vertical motion in our model could be increased by using stronger shear or by developing larger q_T and s_T anomalies for the shear to act upon.

As shown in Fig. 3, the inertial stability field has a midtropospheric maximum with negative regions above and below it, while the potential vorticity field has a midtropospheric maximum. As discussed in Schubert and Hack (1982, 1983), the internal physical processes involved with q_T and s_T are such that as the balanced flow becomes stronger, positive (negative) q_T and s_T anomalies intensify, thus providing greater (lesser) resistance to parcel motion in the vertical and horizontal directions, respectively. In our model simulations these effects are observed in the transverse circulation. For example, the potential vorticity and inertial stability anomalies that develop in a 4-h simulation result in a maximum vertical motion that is less than, by about 10%, its value in the absence of these anomalies. To a similar extent the horizontal ageostrophic flows tend to be suppressed at midlevels and enhanced in the lower and upper troposphere. This mechanism is similar to the

stiffening effect that occurs in tropical cyclones, fronts, and jet stream systems (Schubert and Hack 1983; Hoskins 1974). Finally, from MCS simulations using a full-physics model, G. Tripoli (1996, personal communication) has noted that an inertially stable region, such as in Fig. 3, inhibits entrainment into the sides of an MCS and thus prolongs its existence.

As noted previously, we assumed that the two-dimensional calculation using a nonconstant shear (i.e., the deep or shallow shear in Fig. 2) would result in a small deviation from a three-dimensional calculation. The easiest way to see how three-dimensionality comes into the problem is to examine the transverse circulation equation (2.12a). If $\partial \bar{u}_g / \partial z$ is nonconstant, then the second part of the coefficient A [see (2.12b)] becomes a function of y , that is,

$$\frac{\partial \bar{\theta}}{\partial z} = \frac{f \theta_0 \partial^2 \bar{u}_g}{g \partial z^2} (y - y_0) + \frac{\theta_0 \partial^2 \varphi}{g \partial z^2}, \quad (5.1)$$

from the assumed basic states (the integral in the formula for $\bar{\phi}$ is taken from $y_0 \rightarrow y$). One can easily see that when a constant shear is used, the first term in (5.1) vanishes, and therefore it does not cause any problem. However, when a nonconstant shear is used, the first term is no longer zero. Then $\partial \bar{\theta} / \partial z$ is a function of y , and (2.12a) becomes three-dimensional.

To justify the assumption that we made, let us expand $\bar{\theta}_z$ as the Taylor series at about $y = y_0$:

$$\bar{\theta}_z(y) = \bar{\theta}_z(y_0) + \bar{\theta}'_z(y_0)(y - y_0) + \dots, \quad (5.2)$$

where the superscript prime stands for the partial derivative with respect to y . By comparing (5.1), we obtain

$$\bar{\theta}_z(y_0) = \frac{\theta_0 \partial^2 \varphi}{g \partial z^2},$$

and

$$\bar{\theta}'_z(y_0) = \frac{f \theta_0 \partial^2 \bar{u}_g}{g \partial z^2}.$$

The zeroth-order term [the first term in (5.2)] can be taken as $\bar{\theta}_z(y_0) = 4.5 \text{ K km}^{-1}$ from the *U.S. Standard Atmosphere, 1966* at $y_0 = 30^\circ$ latitude, as we did in the previous section. The first-order term [the second term in (5.2)] can be written as

$$\begin{aligned} \frac{f \theta_0 \partial^2 \bar{u}_g}{g \partial z^2} (y - y_0) &= \frac{\partial}{\partial z} \left(\frac{\partial \bar{\theta}}{\partial y} \right) (y - y_0) \\ &= \frac{1}{\Delta z} \left(\frac{\Delta \bar{\theta}}{\Delta y} \right) \delta y. \end{aligned} \quad (5.3)$$

If we take the standard scaling values as the following, the basic-state temperature change $\Delta \bar{\theta} / \Delta y \sim 10 \text{ K}$ over 1000 km , the depth of atmosphere $\Delta z \sim 10 \text{ km}$, and the mesoscale $\delta y \sim 100 \text{ km}$, we can get the first-order term on an order of 0.1 K km^{-1} . Comparing the value

of the zeroth-order term 4.5 K km^{-1} , the first-order term is about one magnitude smaller.

6. Concluding remarks

The midlatitude squall line has previously been studied both as a slow and a fast manifold phenomenon, as discussed in section 1. Because a squall line is intrinsically a convective problem, such that the excitation of transient inertia-gravity waves is inevitable, the propagation of these waves may play an important role as the squall line evolves (Raymond 1987; Schmidt and Cotton 1990). In fact, scale analysis for these types of systems (Emanuel 1983) has shown that the Rossby and Froude numbers can approach unity. Therefore, primitive-equation models are most appropriate for studying mesoscale problems when solution accuracy is the ultimate goal. However, as a squall line enters its mature stage, characterized by a fully developed midlevel vortex, the local Rossby radius of internal deformation can effectively be decreased, signifying a stronger rotational constraint on the dynamics (Schubert and Hack 1983). In addition, the steady-state assumption (that the convection and precipitation in a squall line are kept relatively constant during its mature stage) made in this study assists to minimize the further spontaneous emission of inertia-gravity waves. These considerations suggest that balanced dynamics becomes increasingly important as a mesoscale convective system enters its mature stage. Under such circumstances some intermediate dynamical models are applicable. The advantage of these balanced models is that they are most amenable to theoretical analysis and physical interpretation.

In this study we employed the Eliassen transverse circulation model derived from the set of semigeostrophic, slab-symmetric equations to study the circulations in a squall line system. Because the semigeostrophic system adopts the geostrophic momentum approximation, as well as retains the ageostrophic advection, circulations with balanced and unbalanced signatures are both present. From this perspective, a midlatitude squall line is viewed as a mesoscale convective system that bridges the large-scale and cloud-convective-scale dynamics. The model used here is well suited to resolving the scale interaction in this kind of problem.

As an alternative formulation of the semigeostrophic theory, the Eliassen transverse circulation model seems to formally emphasize the forced secondary circulation, whereas the PV inversion model (e.g., that used in Herstein and Schubert 1991) more readily describes the balanced flow. In essence, they are the same physical models, both of which can resolve geostrophic and ageostrophic dynamics, either directly or indirectly.

Acknowledgments. Special thanks are extended to Drs. John Brown, Gerald Browning, Richard Johnson, Alexander MacDonald, Michael Montgomery, David

Raymond, Steve Rutledge, and Jerome Schmidt for discussions that clarified many aspects of the paper. Thanks also go to two anonymous reviewers for providing their constructive comments. This work was partially supported by the National Science Foundation, under Grant ATM-9422525.

APPENDIX A

Geostrophic Coordinate Transformation

We now proceed to transform the set of equations (2.1')–(2.5') to geostrophic coordinates, which are defined as $(X, Z, \mathcal{T}) = (x + v_g/f, z, t)$. The physical meaning of this coordinate system can be seen by taking a total derivative of the first entry, then using (2.2') to obtain

$$\frac{DX}{Dt} = \bar{u}_g; \quad (\text{A.1})$$

that is, the horizontal particle displacement in this coordinate is simply related to the basic-state zonal geostrophic wind.

With the transformation relations from (x, z, t) -space to (X, Z, \mathcal{T}) -space

$$\frac{\partial}{\partial x} = \frac{\partial X}{\partial x} \frac{\partial}{\partial X}, \quad (\text{A.2})$$

$$\frac{\partial}{\partial z} = \frac{\partial X}{\partial z} \frac{\partial}{\partial X} + \frac{\partial}{\partial Z}, \quad (\text{A.3})$$

$$\frac{\partial}{\partial t} = \frac{\partial X}{\partial t} \frac{\partial}{\partial X} + \frac{\partial}{\partial \mathcal{T}}, \quad (\text{A.4})$$

we can rewrite the material derivative in the transformed space as

$$\begin{aligned} \frac{D}{Dt} &= \frac{\partial}{\partial t} + (\bar{u}_g + u_{ag} - U) \frac{\partial}{\partial x} + w \frac{\partial}{\partial z} \\ &= \frac{\partial}{\partial \mathcal{T}} + \bar{u}_g \frac{\partial}{\partial X} + w \frac{\partial}{\partial Z}. \end{aligned} \quad (\text{A.5})$$

Thus the geostrophic coordinate transformation makes the horizontal ageostrophic wind and system-relative flow implicit in this coordinate.

By applying (A.2) to the definition of the geostrophic coordinate and noting that $\partial X/\partial x$ is simply the normalized vorticity ζ/f , we can obtain the useful relation

$$\frac{f}{\zeta} = 1 - \frac{1}{f} \frac{\partial v_g}{\partial X}. \quad (\text{A.6})$$

The geostrophic equation (2.1') and the hydrostatic equation (2.3') can be transformed to the new space through the use of (A.2)–(A.4) by defining a new variable $\Phi = \phi + (\frac{1}{2})v_g^2$. This results in

$$\left(f v_g, \frac{g}{\theta_0} \theta \right) = \left(\frac{\partial \Phi}{\partial x}, \frac{\partial \Phi}{\partial z} \right) = \left(\frac{\partial \Phi}{\partial X}, \frac{\partial \Phi}{\partial Z} \right). \quad (\text{A.7})$$

We now define the new ageostrophic flows on the (X, Z) plane as

$$u_{ag}^* = u_{ag} - U + \frac{\Phi_{XZ}}{f^2} w, \quad (\text{A.8})$$

$$w^* = \frac{f}{\zeta} w. \quad (\text{A.9})$$

Using (A.5), (A.7), and the definitions (A.8) and (A.9), we can write the v -momentum equation (2.2') and the thermodynamic equation (2.5') in the transformed space as

$$\frac{\partial v_g}{\partial T} + \bar{u}_g \frac{\partial v_g}{\partial X} + f u_{ag}^* = 0, \quad (\text{A.10})$$

$$\frac{\partial \theta}{\partial T} + \bar{u}_g \frac{\partial \theta}{\partial X} + \frac{\theta_0}{g} (\bar{q} + q) \rho w^* = Q + \frac{f \theta_0 v_g}{g} \frac{\partial \bar{u}_g}{\partial Z}. \quad (\text{A.11})$$

The transformed continuity equation, obtained from the vertical component of the vorticity equation and use of (A.6) and (A.10), takes the same form as in physical space,

$$\frac{\partial u_{ag}^*}{\partial X} + \frac{\partial (\rho w^*)}{\rho \partial Z} = 0, \quad (\text{A.12})$$

which lends itself naturally to define a streamfunction in the (X, Z) plane:

$$(\rho u_{ag}^*, \rho w^*) = \left(-\frac{\partial \psi^*}{\partial Z}, \frac{\partial \psi^*}{\partial X} \right). \quad (\text{A.13})$$

The transformed thermal wind relation is derived from (A.7):

$$f \frac{\partial v_g}{\partial Z} = \frac{g}{\theta_0} \frac{\partial \theta}{\partial X}. \quad (\text{A.14})$$

Finally, with (A.13) and (A.14), (A.10) and (A.11) can be combined to obtain

$$\frac{\partial}{\partial X} \left((\bar{q} + q) \frac{\partial \psi^*}{\partial X} \right) + \frac{\partial}{\partial Z} \left(\bar{s} \frac{\partial \psi^*}{\partial Z} \right) = \frac{g}{\theta_0} \frac{\partial Q}{\partial X} + 2 \rho \bar{s} \frac{\partial \bar{u}_g}{\partial Z}, \quad (\text{A.15a})$$

where

$$q_T = \bar{q} + q = \frac{g}{\rho \theta_0} \frac{\zeta}{f} \frac{\partial}{\partial Z} (\bar{\theta} + \theta), \quad (\text{A.15b})$$

$$s_T = \bar{s} + s = \frac{f}{\rho} \left(f + \frac{\partial v_g}{\partial X} \right). \quad (\text{A.15c})$$

Note that $\bar{s} = \rho^{-1} f^2$ and $s = \rho^{-1} f \partial v_g / \partial X$ are the inertial stability parameters for the basic and perturbed state, respectively.

The boundary conditions for (A.15a) are

$$\begin{aligned} \psi^*(X_L, Z) = \psi^*(X_R, Z) = 0, \\ \psi^*(X, 0) = \psi^*(X, Z_T) = 0. \end{aligned} \quad (\text{A.15d})$$

APPENDIX B

Computational Procedure

The transformed balanced system shown on the right side of Table 1 is numerically integrated using a finite difference procedure as follows. The horizontal domain is partitioned into J equally spaced intervals separated by the $J + 1$ points $X_j = X_L + \Delta X (j = 0, 1, 2, \dots, J)$, while the vertical domain is divided into K equally spaced intervals separated by the $K + 1$ points $Z_k = k \Delta Z (k = 0, 1, 2, \dots, K)$. Staggered midway between the X_j and Z_k points are the points $X_{j+1/2}$ and $Z_{k+1/2}$. The distribution of the variables over these points is shown in Fig. B1. For the results presented in sections 4 and 5 we have chosen $J = 256$, $K = 64$, $\Delta X = 6000$ m, $\Delta Z = 93.75$ m, and $X_L = -960$ km. For these choices the model domain is -960 km $\leq X \leq 960$ km, 0 km $\leq Z \leq 12$ km. Although results are presented only for the region close to the squall line (-300 km $\leq X \leq 300$ km), the relatively large domain size in X is necessary to ensure that the lateral boundary condition (i.e., $u_{ag} = 0$) does not affect the solution in this region of interest.

The solution procedure begins by evaluating the v_g field from the time-dependent variable θ by integration of the thermal wind equation (A.14). Starting this integration with $v_g^* = 0$ at $Z = 0$ yields a v_g^* field, where $v_g = v_g^* - \bar{V}$, and \bar{V} is the integration constant that results from vertically integrating (A.14). This constant is determined at each k with the following formula:

$$\bar{V} = \left[\int_0^{Z_T} \rho v_g^* dz - V_l \right] / \int_0^{Z_T} \rho dz, \quad (\text{B.1})$$

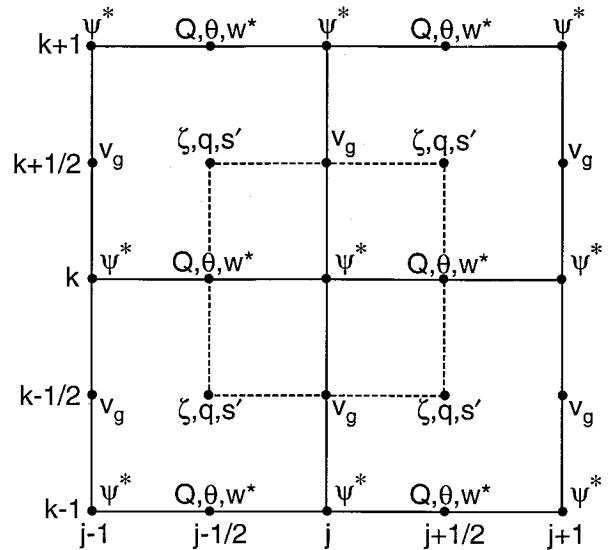


FIG. B1. The finite-difference grid used for solution of the transformed balanced system of equations.

where $V_l = \int_0^{z_T} \rho/v_g dz$ is determined from the vertically integrated form of (A.10),

$$\frac{\partial V_l}{\partial T} = - \int_0^{z_T} \rho \bar{u}_g \frac{\partial v_g}{\partial X} dz, \quad (\text{B.2})$$

using a second-order Adams–Bashforth scheme in time and assuming $V_l = 0$ at $T = 0$. For the case where $\bar{u}_g = 0$, we note that V_l (i.e., the vertically integrated, mass-weighted v_g field) is identically zero at all times. Having determined v_g , we then diagnose the normalized absolute vorticity ζ/f , potential vorticity q , and inertial stability s , using (A.6), (A.15b), and (A.15c), respectively. The heating, which is specified in physical space (4.1), is transformed into geostrophic space using the coordinate transformation defined at the beginning of section 3. The transverse circulation equation (A.15a) is then used to diagnose ψ^* . Likewise, (A.13) is used to diagnose u_{ag}^* and w^* . Finally, (A.11) is used to predict a new θ .

The numerical methods for the computations described here are all based upon second-order centered differences. Where necessary (i.e., near or at boundaries) one-sided, second-order differences were used. For the transverse circulation equation, the discrete approximation is written as

$$\begin{aligned} & \alpha_{j-1/2,k} \psi_{j-1,k}^* - (\alpha_{j-1/2,k} + \alpha_{j+1/2,k}) \psi_{j,k}^* + \alpha_{j+1/2,k} \psi_{j+1,k}^* \\ & + \beta_{j,k-1/2} \psi_{j,k-1}^* - (\beta_{j,k-1/2} + \beta_{j,k+1/2}) \psi_{j,k}^* \\ & + \beta_{j,k+1/2} \psi_{j,k+1}^* = \frac{g}{\theta_0} \left(\frac{\partial Q}{\partial X} \right)_{j,k} + \rho_k s'_{j,k} \left(\frac{\partial \bar{u}_g}{\partial Z} \right)_k, \end{aligned} \quad (\text{B.3})$$

where

$$\alpha_{j-1/2,k} = (q_{j-1/2,k+1/2} + q_{j-1/2,k-1/2}) / (2\Delta X^2)$$

$$\beta_{j,k-1/2} = \bar{s}_{k-1/2} / \Delta Z^2$$

$$\begin{aligned} s'_{j,k} &= (s'_{j+1/2,k+1/2} + s'_{j+1/2,k-1/2} \\ &+ s'_{j-1/2,k+1/2} + s'_{j-1/2,k-1/2}) / 4. \end{aligned}$$

The prediction of θ with (A.11) uses a forward scheme at the first time step and a second-order Adams–Bashforth scheme at subsequent times as shown here:

$$\theta_{j+1/2,k}^{n+1} = \theta_{j+1/2,k}^n + \Delta T F_{j+1/2,k}^n \quad \text{for } n = 0 \quad (\text{B.4})$$

$$\begin{aligned} \theta_{j+1/2,k}^{n+1} &= \theta_{j+1/2,k}^n \\ &+ \frac{\Delta T}{2} (3F_{j+1/2,k}^n - F_{j+1/2,k}^{n-1}) \quad \text{for } n \geq 1, \end{aligned} \quad (\text{B.5})$$

where

$$\begin{aligned} F_{j+1/2,k} &= -\bar{u}_{gk} \left(\frac{\theta_{j+3/2,k} - \theta_{j-1/2,k}}{2\Delta X} \right) \\ &- \frac{\theta_0}{g} \left(\frac{q_{j+1/2,k+1/2} + q_{j+1/2,k-1/2}}{2} \right) \rho_k w_{j+1/2,k}^* + Q_{j+1/2,k} \\ &+ \frac{f\theta_0}{g} \left(\frac{v_{g_{j+1,k+1/2}} + v_{g_{j,k+1/2}} + v_{g_{j+1,k-1/2}} + v_{g_{j,k-1/2}}}{4} \right) \left(\frac{\partial \bar{u}_g}{\partial z} \right)_{j+1/2,k}. \end{aligned}$$

For the spatial resolution mentioned above, a time step ΔT of 100 seconds was sufficient to avoid computational instability.

The solution of (B.3) was accomplished using a multigrid solver with alternating-direction zebra relaxation. This solver is quite similar to that used in Ciesielski et al. (1986) to solve the transverse-circulation equation for a tropical cyclone. For the resolution described earlier, convergence of the solution to below truncation error is obtained with the equivalent of six iteration sweeps (which takes 1.1 s on an HP Apollo 9000 Model 730 workstation).

REFERENCES

- Biggerstaff, M. I., and R. A. Houze Jr., 1991: Kinematic and precipitation structure of the 10–11 June 1985 squall line. *Mon. Wea. Rev.*, **119**, 3034–3065.
- Ciesielski, P. E., S. R. Fulton, and W. H. Schubert, 1986: Multigrid solution of an elliptic boundary value problem from tropical cyclone theory. *Mon. Wea. Rev.*, **114**, 797–807.
- Eliassen, A., 1962: On the vertical circulation in frontal zones. *Geophys. Publ.*, **24**, 147–160.
- Emanuel, K. A., 1979: Inertial instability and mesoscale convective systems. Part I: Linear theory of inertial instability in rotating viscous fluids. *J. Atmos. Sci.*, **36**, 2425–2499.
- , 1983: On the dynamical definitions of mesoscale. *Mesoscale Meteorology: Theories, Observations and Models*, D. K. Lilly and T. Gal-Chen, Eds., Reidel Publishing, 1–11.
- Davis, C. A., and M. L. Weisman, 1994: Balanced dynamics of mesoscale vortices produced in simulated convective systems. *J. Atmos. Sci.*, **51**, 2005–2030.
- Fovell, R. G., and Y. Ogura, 1988: Numerical simulation of a mid-latitude squall line in two dimensions. *J. Atmos. Sci.*, **45**, 3846–3879.
- Gallus, W. A., Jr., and R. H. Johnson, 1991: Heat and moisture budgets of an intense midlatitude squall line. *J. Atmos. Sci.*, **48**, 122–146.

- , and —, 1992: The momentum budget of an intense midlatitude squall line. *J. Atmos. Sci.*, **49**, 422–450.
- Hack, J. J., W. H. Schubert, D. E. Stevens, and H.-C. Kuo, 1989: Response of the Hadley circulation to convective forcing in the ITCZ. *J. Atmos. Sci.*, **46**, 2957–2973.
- Haynes, P. H., and M. E. McIntyre, 1987: On the evolution of vorticity and potential vorticity in the presence of diabatic heating and frictional or other forces. *J. Atmos. Sci.*, **44**, 828–841.
- Hertenstein, R. F. A., and W. H. Schubert, 1991: Potential vorticity anomalies associated with squall lines. *Mon. Wea. Rev.*, **119**, 1663–1672.
- Hoskins, B. J., 1974: The role of potential vorticity in symmetric stability and instability. *Quart. J. Roy. Meteor. Soc.*, **100**, 480–482.
- , 1975: The geostrophic momentum approximation and the semi-geostrophic equations. *J. Atmos. Sci.*, **32**, 233–242.
- , and I. Draghici, 1977: The forcing of ageostrophic motion according to the semi-geostrophic equations and in an isentropic coordinate model. *J. Atmos. Sci.*, **34**, 1859–1867.
- , M. E. McIntyre, and A. W. Robertson, 1985: On the use and significance of isentropic potential vorticity maps. *Quart. J. Roy. Meteor. Soc.*, **111**, 877–946.
- Houze, R. A., Jr., S. A. Rutledge, M. I. Biggerstaff, and B. F. Smull, 1989: Interpretation of Doppler weather radar displays of midlatitude mesoscale convective systems. *Bull. Amer. Meteor. Soc.*, **70**, 608–619.
- Jiang, H., and D. J. Raymond, 1995: Simulation of a mature mesoscale convective system using a nonlinear balance model. *J. Atmos. Sci.*, **52**, 161–175.
- Johnson, R. H., and P. J. Hamilton, 1988: The relationship of surface pressure features to the precipitation and air flow structure of an intense midlatitude squall line. *Mon. Wea. Rev.*, **116**, 1444–1472.
- Menard, R. D., and J. M. Fritsch, 1989: A mesoscale convective complex-generated inertially stable warm core vortex. *Mon. Wea. Rev.*, **117**, 1237–1261.
- Moncrieff, M. W., 1978: The dynamical structure of two-dimensional steady state convection in constant vertical shear. *Quart. J. Roy. Meteor. Soc.*, **104**, 543–567.
- Ogura, Y., and M.-T. Liou, 1980: The structure of a midlatitude squall line: A case study. *J. Atmos. Sci.*, **37**, 553–567.
- Raymond, D. J., 1987: A forced gravity wave model of self-organized convection. *J. Atmos. Sci.*, **44**, 3528–3543.
- , and H. Jiang, 1990: A theory for long-lived mesoscale convective systems. *J. Atmos. Sci.*, **47**, 3067–3077.
- Rotunno, R., J. B. Klemp, and M. L. Weisman, 1988: A theory for strong, long-lived squall lines. *J. Atmos. Sci.*, **45**, 463–485.
- Rutledge, S. A., R. A. Houze Jr., M. I. Biggerstaff, and T. Matejka, 1988: The Oklahoma–Kansas mesoscale convective system of 10–11 June 1985: Precipitation structure and single-Doppler radar analysis. *Mon. Wea. Rev.*, **116**, 1409–1430.
- Schmidt, J. M., and W. R. Cotton, 1990: Interactions between upper and lower tropospheric gravity waves on squall line structure and maintenance. *J. Atmos. Sci.*, **47**, 1205–1222.
- Schubert, W. H., 1985: Semigeostrophic theory. *J. Atmos. Sci.*, **42**, 1770–1772.
- , and J. J. Hack, 1982: Inertial stability and tropical cyclone development. *J. Atmos. Sci.*, **39**, 1687–1697.
- , and —. 1983: Transformed Eliassen balanced vortex model. *J. Atmos. Sci.*, **40**, 1571–1583.
- , S. R. Fulton, and R. F. A. Hertenstein, 1989: Balanced atmospheric response to squall lines. *J. Atmos. Sci.*, **46**, 2478–2483.
- Smull, B. F., and R. A. Houze, 1987: Rear inflow in squall lines with trailing stratiform precipitation. *Mon. Wea. Rev.*, **115**, 2869–2889.
- Thorpe, A. J., M. J. Miller, and M. W. Moncrieff, 1982: Two-dimensional convection in nonconstant shear: A model of midlatitude squall lines. *Quart. J. Roy. Meteor. Soc.*, **108**, 739–762.
- Weisman, M. L., 1992: The role of convectively generated rear-inflow jets in the evolution of long-lived mesoconvective systems. *J. Atmos. Sci.*, **49**, 1826–1847.
- Zhang, D.-L., and K. Gao, 1989: Numerical simulation of an intense squall line during 10–11 June 1985 PRE-STORM. Part II: Rear inflow, surface pressure perturbations and stratiform precipitation. *Mon. Wea. Rev.*, **117**, 2067–2094.